Pulse-Doppler Signal Processing With Quadrature Compressive Sampling

CHAO LIU
FENG XI, Member, IEEE
SHENGYAO CHEN, Member, IEEE
Nanjing University of Science and Technology
Nanjing, Jiangsu, China

YIMIN D. ZHANG, Senior Member, IEEE
Villanova University
Villanova, PA, USA

ZHONG LIU, Member, IEEE
Nanjing University of Science and Technology
Nanjing, Jiangsu, China

Quadrature compressive sampling (QuadCS) is a recently introduced sub-Nyquist sampling scheme for effective acquisition of inphase and quadrature (I/Q) components of sparse radio frequency signals. In applications to pulse-Doppler radars, the QuadCS outputs can be arranged into a two-dimensional data format, in terms of slow time and virtual fast time, similar to that by Nyquist sampling. This paper develops a compressive sampling pulse-Doppler (CoSaPD) processing scheme which performs Doppler estimation/detection and range estimation from the sub-Nyquist data without recovering the Nyquist samples. The Doppler estimation is realized through a spectrum analyzer as in classical processing, whereas the detection is performed using the Doppler bin data. The range estimation is performed using sparse recovery algorithms only for the detected targets to reduce the computational load. A low detection threshold is used to improve the detection probability and the introduced false targets are then removed in the range estimation stage by exploiting the inherent target detection capability of the recovery algorithms. Simulation results verify the effectiveness of the proposed CoSaPD scheme, which requires only one-eighth of the Nyquist rate to achieve similar performance to the classical processing with Nyquist samples, provided that the input signal-to-noise ratio (SNR) is above −25 dB.

I. INTRODUCTION

Pulse-Doppler processing has found wide applications in civilian and military air surveillance radars due to its capability to detect moving targets in strong clutter environments by exploiting the distinct Doppler shifts between the targets and the clutter [1, 2]. A common processing scheme uses a quadrature sampling structure [3, 4], as shown in Fig. 1, where the radar echoes are sampled to obtain baseband inphase and quadrature (denoted by I and Q) components. After processing the baseband signal through a matched filter and discrete Fourier transform (DFT), a detection threshold is applied to detect targets with a constant false alarm rate (CFAR). The detected target plots are then fed into the data processor to perform tracking and other functions.

Assume that the radar echoes are downconverted into an intermediate frequency (IF) of f_0 with a bandwidth of B. Then, the Nyquist sampling rate for the analog-to-digital conversion (ADC) is given by [5]

$$f_s = \frac{4f_L + 2B}{4l + 1}$$

where $f_L = f_0 - B/2$, and l is a positive integer satisfying $l \leq \lfloor f_L/2B \rfloor$, where $\lfloor \cdot \rfloor$ denotes the floor function. In wideband and ultrawideband applications, therefore, high-rate ADC and, subsequently, intensive processing of high dimensional sequences are required. As a result, the current availability of the ADC technologies limits the development of high-resolution ultrawideband radar systems.

The recently introduced compressed sensing (CS) [6–8], or compressive sampling, techniques bring us new concepts to achieve sub-Nyquist data acquisition. The CS theory exploits the signal sparsity and samples signals closer to their information rate instead of their bandwidth. With a high probability, CS techniques recover sparse signals from far fewer samples or measurements than the Nyquist samples. In radar systems, the reduced number of samples implies a lower sampling rate requirement and, hence, a reduced processing load. While the CS theory is developed primarily for discrete-domain signals, several schemes, such as random sampling [9], random demodulation [10, 11], random-modulation preintegrator (RMPI) [12], segmented compressed sampling [13], and Xampling [14], have been proposed to apply CS techniques to analog signals, known as analog-to-information conversion (AIC). These schemes, which generally handle signals that are sparse in the time domain, frequency domain, or time-frequency domain, are studied for bandpass signals without exploiting the characteristics of radar signals by extracting the I and Q components from the IF waveforms.

Recently, we proposed a quadrature compressive sampling (QuadCS) scheme [15, 16] that bridges the CS theory and the digital quadrature sampling. By assuming the sparsity of the echo signals in the waveform-matched dictionary [17], the QuadCS can directly extract the I and
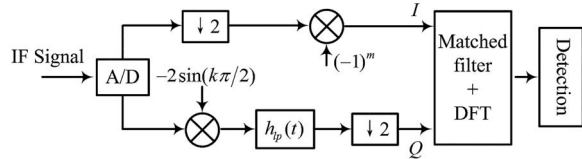
Fig. 1. Block schematic of classical processing.

Q components of the bandpass signals and, similar to the random demodulation scheme, demodulate the signals through the chipping sequences. The chipping rate, however, is determined by the bandwidth, rather than the highest frequency, of the bandpass signals. Therefore, the QuadCS reduces the implementation complexity as compared with the random demodulation scheme.

It is noted that the digital signals obtained through the AIC are sparse and thus differ from those obtained from the uniform Nyquist sampling. As a result, the conventional signal processing techniques cannot be directly applied to them for information extraction. In general, there are two fundamental approaches to perform the information processing. One is to first recover the Nyquist sampling signals and then process the recovered signals using conventional methods. It is clear, therefore, that this type of processing does not fully take advantage of sub-Nyquist sampling, i.e., it has to deal with a large volume of recovered data represented in the Nyquist rate. The other approach is to directly process the sparse signals, which have a much smaller size, in the CS domain. Signal processing in the CS domain, also referred to as compressive signal processing (CSP), is attractive due to its capability of significant reduction to the overall processing complexity. Some fundamental works, for example, signal detection, parameter estimation, and filtering, have been reported in, e.g. [18, 19]. In comparison with conventional techniques, CSP is still in its infancy and much work should be done before it is applied in practice.

In this paper, we discuss the applications of the QuadCS scheme to radar applications and develop the compressive sampling pulse-Doppler (CoSaPD) processing approach. We are mainly concerned with nonfluctuating moving point targets in the presence of additive white Gaussian noise (AWGN). The application of the proposed CoSaPD in cluttered environments is also discussed in less detail. It is assumed that the radar transmits repetitive pulse trains, and the target echoes are sampled at a sub-Nyquist rate in the fast-time (range) domain using the QuadCS. In the Doppler dimension, the target echoes are sampled at the pulse repetition frequency. Then, in a coherent processing interval (CPI), the sampled data can be formulated in a matrix similar to that with the classical sampling, as described in Section IV [1, 2]. Because of the reduced-rate intrapulse sampling, the yielding data size becomes much smaller. The complete target information (amplitudes, Doppler frequencies, and ranges) is contained in the compressive data matrix, based

on which target detection and estimation can be performed. The CoSaPD scheme consists of the procedures of Doppler estimation, target detection, and range estimation. As discussed in Section V, the order of the procedures is irreversible, which is different from the classical processing. Simulation results in Section VI show that, when the input signal-to-noise ratio (SNR) is above -25 dB, the CoSaPD scheme at one-eighth of the Nyquist rate achieves a performance similar to that obtained by classical processing methods using Nyquist sampled data.

Applications of AIC and CSP to radar systems have been exploited in, e.g. [12, 20–27]. In [12], an RMPI-based radar pulse receiver is reported that extracts target information without full signal reconstruction. Target detection from sub-Nyquist samples is considered in [20, 21]. Target tracking and time-delay/Doppler estimation from random measurements are respectively studied in [22] and [23]. In [24], the reconstruction performance of radar echoes is examined using real experimental data. References [25–27] present different approaches for the estimation of radar target parameters from Xampling data. All these studies demonstrate the effectiveness of the AIC for effective radar signal acquisition with a significantly reduced complexity. In this paper, we further consolidate the applicability of the AIC to radar systems. Different from previous work, the CoSaPD is a systematic pulse-Doppler processing scheme based on QuadCS. Owing to the data structure parallel to the Nyquist sampling, the CoSaPD takes some ideas from the classical processing but with different connotations of the QuadCS data. As such, the target detection and range estimation adopt different techniques, as discussed in Section IV. Other contributions of this paper include analyses of detection performance, joint detection and range estimation with a low detection threshold, and extensive performance evaluations in different scenarios.

The remainder of this paper is organized as follows. In Section II we describe the radar model and the assumptions used in our discussion. Section III briefly summarizes the fundamentals of the QuadCS scheme. Section IV describes the proposed CoSaPD processing scheme, and the target detection approach is discussed in Section V. Simulation results are presented in Section VI. We conclude this paper in Section VII.

We denote vectors by boldface lower case letters and matrices by boldface upper case letters. $(\bullet)^H$ denotes the conjugate transpose operation. $(\bullet)^l$ denotes the l-th column of matrix "$\bullet$", and $(\bullet)_{i,j}$ denotes the element of "$\bullet$" in the i-th row and j-th column. Re $\{\bullet\}$ and Im $\{\bullet\}$ represent the real and the imaginary parts of "$\bullet$", respectively.

II. RADAR MODEL AND PROBLEM STATEMENT

In pulse-Doppler radar signal processing, we usually transmit repetitive periodic pulses and perform coherent sampling at the range bins so as to estimate desirable target information. Consider the case of K nonfluctuating moving point targets which are sparsely located in the

radar's field of view and satisfy the stop-and-hop assumption [1]. Assume that the radar transmits a modulated pulse train with L pulses, where the pulse repetition interval (PRI) is T and the pulsewidth is T_b. After downconverting the received signal to an IF of f_0, the target echo from the k-th target corresponding to the l-th transmit pulse can be described as

$$r_k^l(t) = \rho_k a(t - t_k) \cos[2\pi f_0 t + \phi(t - t_k) \\ + 2\pi f_k^d (l-1)T + \varphi_k], \ t \in [(l-1)T, lT], \quad (1)$$

where $a(t)$ and $\phi(t)$ respectively represent the amplitude and the phase of the transmitted signal, which has a bandpass spectrum with center frequency f_0 and bandwidth B. In addition, ρ_k, t_k, f_k^d, and φ_k are the reflecting coefficient, time delay, Doppler frequency, and random phase shift of the k-th target, respectively. In the presence of K targets, the received radar echo corresponding to the l-th transmit pulse is the superposition of their respective echoes and can be expressed as

$$r^l(t) = \sum_{k=1}^{K} r_k^l(t) = I^l(t) \cos(2\pi f_0 t) - Q^l(t) \sin(2\pi f_0 t) \\ (2)$$

where $I^l(t)$ and $Q^l(t)$ are respectively the I and Q components of the signal $r^l(t)$, i.e.,

$$I^l(t) = \sum_{k=1}^{K} \rho_k a(t - t_k) \cos[\phi(t - t_k) + \varphi'_k] \\ (3)$$
$$Q^l(t) = \sum_{k=1}^{K} \rho_k a(t - t_k) \sin[\phi(t - t_k) + \varphi'_k]$$

and $\varphi'_k = 2\pi f_k^d (l-1)T + \varphi_k$. Denote $\tilde{s}_0(t) = a(t)e^{j\phi(t)}$ as the complex baseband signal of the transmitted radar signal. Then the complex envelope $\tilde{s}^l(t)$ of $r^l(t)$ is given by

$$\tilde{s}^l(t) = I^l(t) + jQ^l(t) = \sum_{k=1}^{K} \tilde{\rho}_k^l \tilde{s}_0(t - t_k) \quad (4)$$

where $\tilde{\rho}_k^l = \rho_k \exp[j(2\pi f_k^d (l-1)T + \varphi_k)]$.

The target information, characterized by t_k, f_k^d, and ρ_k, is completely contained in the complex baseband envelope $\tilde{s}^l(t)$, $l = 1, 2, \cdots, L$. In the radar signal processing, we usually sample $r^l(t)$ in (2) by the quadrature sampling scheme and then perform the analysis to obtain the target information, as shown in Fig. 1. On the other hand, this paper studies the estimation of target information from the sub-Nyquist QuadCS data.

To simplify the analysis without loss of generality, we assume that the radar is operated in an unambiguous time-frequency region, i.e., $|f_d| < 1/2T$ and $t_k < T$, and that the target remains in a range bin and keeps a constant velocity in a CPI.

In practical scenarios, the received radar signal inevitably contains noise and clutter in addition to the

target echoes.[1] Among various noise sources, thermal noise is nominally dominant. Clutter is often present due to echoes from volume or surface scatterers [28]. In our study, we assume that the noise is AWGN and the surface clutter is Rayleigh distributed in amplitude and obeys the two-sided exponential law in Doppler spreading. Then, the received radar signal corresponding to the l-th transmitting pulse is given by

$$r^l(t) = \sum_{k=1}^{K} r_k^l(t) + n(t) + c(t), \ t \in [(l-1)T, lT], \quad (5)$$

where $n(t)$ is the bandlimited noise with power spectrum density $N_0/2$ and bandwidth B, and $c(t)$ is Rayleigh-distributed clutter with an average clutter power of ρ_c^2. Define the received SNR for the k-th target as

$$\text{SNR}_k^{IN} = \frac{\frac{1}{T_b} \int_{(l-1)T}^{lT} |r_k^l(t)|^2 \, dt}{N_0 B}. \quad (6)$$

We can obtain that $\text{SNR}_k^{IN} = \frac{|\rho_k|^2}{N_0 B}$ under the assumption of unit transmit power. Similarly, the received signal-to-clutter ratio (SCR) can be defined for the k-th target as $\text{SCR}_k^{IN} = \frac{|\rho_k|^2}{\rho_c^2}$.

In the rest of the paper, we consider the case of target echoes contaminated only by the thermal noise $n(t)$. The effects of clutter are analyzed in Section IV and simulation results are provided in Section VI.

III. FUNDAMENTALS OF QUADRATURE COMPRESSED SENSING

Now we introduce the QuadCS scheme that performs sub-Nyquist sampling of the received radar signal as expressed in (5). Different from the system in [15, 16], this work takes the Doppler into account in the echo model. To simplify the notation, we consider the received signal, denoted as $r(t)$, in a single pulse interval.

We first consider the noise-free case. In radar applications, because the transmit waveforms are known in advance, a natural choice of the dictionary is to use entries that are matched with the transmit waveforms [17]. For baseband radar CS processing with transmit waveform $\tilde{s}_0(t)$ of bandwidth B, the waveform-matched dictionary consists of time-delayed versions of $\tilde{s}_0(t)$ at all integral multiples of $\tau_0 = 1/B$, i.e., $\{\tilde{\psi}_n(t) | \tilde{\psi}_n(t) = \tilde{s}_0(t - n\tau_0), n = 0, 1, \cdots, N-1\}$, where $N = \lceil T/\tau_0 \rceil$ is the size of the dictionary, with $\lceil \cdot \rceil$ denoting the ceiling function. As such, the dictionary discretizes the observation time period T with resolution $\tau_0 = 1/B$. This discretization of the time delay is justified by the fact that the time resolution of the bandlimited signal $\tilde{s}_0(t)$ is $1/B$.

Assume that the target delays are located at the integral multiples of $\tau_0 = 1/B$, i.e., $t_k \in \{0, \tau_0, \cdots, (N-1)\tau_0\}$. Given the waveform-matched dictionary, the complex

---

[1] Unintentional electromagnetic interference and intentional jamming are out of the scope of our discussion.
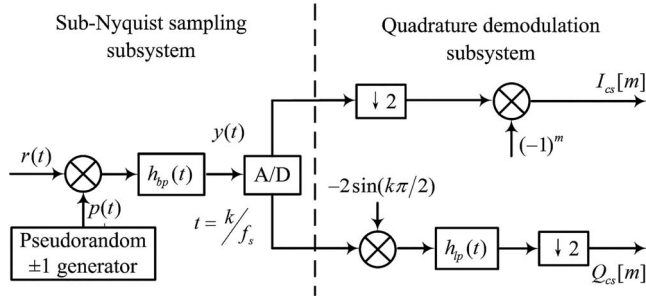
Fig. 2. Structure of QuadCS system.

envelope $\tilde{s}(t)$ in (4) can be represented as

$$\tilde{s}(t) = \sum_{n=0}^{N-1} \tilde{\rho}_n \tilde{\psi}_n(t), \qquad (7)$$

where $\tilde{\rho}_k$ is the target reflection coefficient that takes a nonzero value at delay t_k. For $K \ll N$, $\tilde{s}(t)$ is said to be K-sparse in the waveform-matched dictionary. The sparsity level K exactly equals to the number of targets.

The QuadCS system is shown in Fig. 2, which consists of two subsystems: a sub-Nyquist sampling subsystem and a quadrature demodulation subsystem. In the first subsystem, the received radar signal $r(t)$ is modulated by a random chipping sequence $p(t)$ of ± 1s, which alternates between values at or above the Nyquist rate of the baseband signal. The mixer operation spreads the baseband signal content to occupy the full spectrum of $p(t)$. Then, the mixed output is filtered by a bandpass filter $h_{bp}(t)$ with a center frequency f_0 and bandwidth $B_{cs} \ll B$. The filter output yields a compressive bandpass signal, expressed as

$$y(t) = \int_{-\infty}^{\infty} h_{bp}(\tau) p(t-\tau) r(t-\tau) d\tau$$
$$= \text{Re}\left\{\tilde{s}_{cs}(t) e^{j2\pi f_0 t}\right\} \qquad (8)$$

where

$$\tilde{s}_{cs}(t) = \int_{-\infty}^{+\infty} h_{bp}(\tau) e^{-j2\pi f_0 \tau} p(t-\tau) \tilde{s}(t-\tau) d\tau \quad (9)$$

is the compressive complex envelope, with $I_{cs}(t) = \text{Re}\{\tilde{s}_{cs}(t)\}$ and $Q_{cs}(t) = \text{Im}\{\tilde{s}_{cs}(t)\}$ denoting the compressive I and Q components, respectively. The filter output $y(t)$ is then sampled by a sub-Nyquist ADC to generate a low-rate sequence $y[k]$. The sampling rate is set according to the bandpass sampling theorem as $f_{IF}^{cs} = (4f_L + 2B_{cs})/(4l+1)$, where $f_L = f_0 - B_{cs}/2$, and l is a positive integer satisfying $l \le \lfloor f_L/2B_{cs} \rfloor$.

The second subsystem is to extract digital compressive I and Q sequences from the sub-Nyquist sampling sequence $y[k]$. Its operation is the same as in classical quadrature sampling [3]. Because of the down-sampling operation, the rate of the digital compressive I and Q sequences $I_{cs}[m] = I_{cs}(mT_{cs})$ and $Q_{cs}[m] = Q_{cs}(mT_{cs})$ is half that of $y[k]$, i.e., $T_{cs} = 2/f_{IF}^{cs}$. In the observation interval T, we obtain $M = \lfloor T/T_{cs} \rfloor$ complex samples

$\tilde{s}_{cs}[m] = I_{cs}[m] + jQ_{cs}[m]$, or $2M$ compressive samples of I and Q components, from $\tilde{s}_{cs}(t)$, which are much less than $2BT$ as required by the digital quadrature demodulation.

Although the QuadCS system works on analog bandpass signals, its output $s_{cs}[m]$ can be characterized as a linear combination of the elements of sparse coefficient vector $\tilde{\rho} = [\tilde{\rho}_0, \tilde{\rho}_1, \cdots, \tilde{\rho}_{N-1}]^T$. Substituting (7) into (9), we have

$$\tilde{s}_{cs}(t)$$
$$= \sum_{n=0}^{N-1} \tilde{\rho}_n \int_{-\infty}^{+\infty} h_{bp}(\tau) e^{-j2\pi f_0 \tau} p(t-\tau) \tilde{\psi}_n(t-\tau) d\tau \qquad (10)$$

and the corresponding samples are expressed as

$$\tilde{s}_{cs}[m] = \sum_{n=0}^{N-1} \tilde{\rho}_n \int_{-\infty}^{+\infty} h_{bp}(\tau) e^{-j2\pi f_0 \tau} p(mT_{cs} - \tau)$$
$$\times \tilde{\psi}_n(mT_{cs} - \tau) d\tau. \qquad (11)$$

In the discrete CS framework, we have

$$\tilde{s}_{cs} = \tilde{M}\tilde{\rho} \qquad (12)$$

where $\tilde{s}_{cs} = [\tilde{s}_{cs}[0], \cdots, \tilde{s}_{cs}[M-1]]^T$ and $\tilde{M} = [\tilde{M}_{mn}] \in \mathbb{C}^{M \times N}$ with

$$\tilde{M}_{mn} = \int_{-\infty}^{+\infty} h_{bp}(\tau) e^{-j2\pi f_0 \tau} p(mT_{cs} - \tau)$$
$$\times \tilde{\psi}_n(mT_{cs} - \tau) d\tau. \qquad (13)$$

The recovery of the sparse coefficient vector $\tilde{\rho}$ can be achieved through the following constrained l_1-norm optimization [29]

$$\begin{cases} \min \ \|\tilde{\rho}\|_1 \\ \text{s.t. } \tilde{s}_{cs} = \tilde{M}\tilde{\rho} \end{cases} \qquad (14)$$

In the above expression, matrix $\tilde{M}$ is referred to as the system measurement matrix. For radar signals with a flat spectrum, all the columns of matrix $\tilde{M}$ are approximately mutually orthogonal and have nearly the same column energy $2T_b B_{cs}^2/B$ under the assumption of unit transmit power. Therefore, the k-th target power after the output of the QuadCS system becomes $2|\rho_k|^2 B_{cs}/B$.

When the received signals are contaminated by noise, the QuadCS samples in (11) are corrupted by compressive noise samples $\tilde{n}_{cs}[m]$, which are obtained by passing the received noise $n(t)$ through the QuadCS system as described above. For the additive white and bandlimited Gaussian noise $n(t)$ with power spectrum density $N_0/2$ and bandwidth B, the compressive noise samples $\tilde{n}_{cs}[m]$ are an independent and identically distributed (IID) complex Gaussian process with zero-mean and variance $2N_0 B_{cs}$ [30]. Then, the output SNR of the QuadCS system for the k-th target, denoted as SNR_k^{CS}, stays intact.

Because the QuadCS is a linear system, (12) becomes

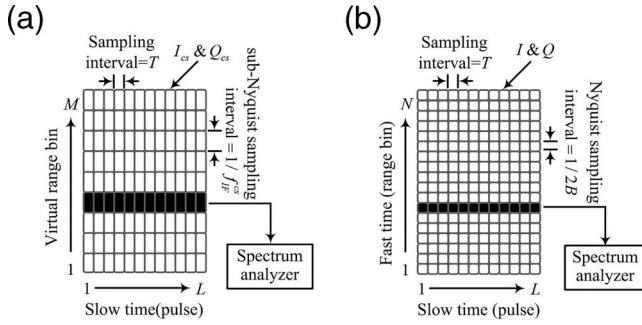$$\tilde{s}_{cs} = \tilde{M}\tilde{\rho} + \tilde{n}_{cs} \qquad (15)$$

Fig. 3. Notional two-dimensional data matrix generated by (a) QuadCS system and (b) classical sampling.

in the noisy case, where $\tilde{\mathbf{n}}_{cs} = [\tilde{n}_{cs}[0], \cdots, \tilde{n}_{cs}[M-1]]^T$. The reconstruction of the sparse coefficient vector $\tilde{\boldsymbol{\rho}}$ in this case can be obtained as the solution of the following optimization problem [31],

$$\min_{\tilde{\boldsymbol{\rho}}} \frac{1}{2} \left\| \tilde{\mathbf{s}}_{cs} - \tilde{\mathbf{M}} \tilde{\boldsymbol{\rho}} \right\|_2^2 + \lambda \left\| \tilde{\boldsymbol{\rho}} \right\|_1, \tag{16}$$

where $\lambda > 0$ is the regularization parameter which is used to tradeoff between the sparsity and the least-squares errors.

There are a wide variety of approaches to solve (14) and (16), including the greedy iteration algorithms [32, 33] and convex optimization algorithms [31, 34] (see [35] for a review). In the simulation study, we use basis pursuit denoising (BPDN) [31] to estimate the sparse vector $\tilde{\boldsymbol{\rho}}$.

IV. PULSE-DOPPLER PROCESSING IN QUADCS DOMAIN

In this section, we discuss the extraction of the target range and Doppler frequency information from the data expressed in (15).

Consider a CPI consisting of L periodic pulses and denote the output of the QuadCS system from the l-th echo as

$$\tilde{\mathbf{s}}_{cs}^l = \tilde{\mathbf{M}} \tilde{\boldsymbol{\rho}}^l + \tilde{\mathbf{n}}_{cs}^l. \tag{17}$$

Define $\tilde{\mathbf{S}}_{cs} = [\tilde{\mathbf{s}}_{cs}^1, \tilde{\mathbf{s}}_{cs}^2, \cdots, \tilde{\mathbf{s}}_{cs}^L]$, $\tilde{\boldsymbol{\Theta}} = [\tilde{\boldsymbol{\rho}}^1, \tilde{\boldsymbol{\rho}}^2, \cdots, \tilde{\boldsymbol{\rho}}^L]$, and $\tilde{\mathbf{N}}_{cs} = [\tilde{\mathbf{n}}_{cs}^1, \tilde{\mathbf{n}}_{cs}^2, \cdots, \tilde{\mathbf{n}}_{cs}^L]$. Then, the sampled data of the L consecutive echoes can be expressed in a matrix form as

$$\tilde{\mathbf{S}}_{cs} = \tilde{\mathbf{M}} \tilde{\boldsymbol{\Theta}} + \tilde{\mathbf{N}}_{cs}. \tag{18}$$

Fig. 3(a) illustrates the two-dimensional data matrix generated by the QuadCS system, whereas Fig. 3(b) depicts that by the classical sampling [1, 2] for comparison. It is clear that the sub-Nyquist samples obtained by the QuadCS system correspond to the fast time samples (range bins) in the classical sampling. As such, the sub-Nyquist samples are referred to as the virtual range bins for convenience. The samples in each column are obtained by successively sampling the echoes from a single pulse, yielding consecutive virtual range bins. Each complex element of a column represents both real and imaginary (I_{cs} and Q_{cs}) components for one virtual range

bin. Consequently, each row represents a series of measurements from the same virtual range bin over consecutive pulses. Because of the reduced sub-Nyquist rate in the range dimension, the data size in the range dimension becomes much smaller than that obtained by the classical fast-time Nyquist sampling.

As can be seen from (18), the target information is completely characterized by the $N \times L$ data matrix $\tilde{\boldsymbol{\Theta}}$. In fact, matrix $\tilde{\boldsymbol{\Theta}}$ degenerates to the classical data matrix when $\tilde{\mathbf{M}} = \mathbf{I}_N$. Then, $\tilde{\boldsymbol{\Theta}}$ can be obtained by estimating the target information similar to traditional approaches. However, because the available data is an $M \times L$ underdetermined data matrix $\tilde{\mathbf{S}}_{cs}$ with $M \ll N$, it is impossible to directly obtain the target information from $\tilde{\mathbf{S}}_{cs}$. Ideally, each column of $\tilde{\boldsymbol{\Theta}}$ is sparse because the number of targets is much smaller than that of the range bins or the dictionary size. In this case, we can obtain a sparse estimate of $\tilde{\boldsymbol{\Theta}}$ in (18) by solving the following l_1-norm optimization problem,

$$\min_{\tilde{\boldsymbol{\rho}}^l} \frac{1}{2} \left\| \tilde{\mathbf{s}}_{cs}^l - \tilde{\mathbf{M}} \tilde{\boldsymbol{\rho}}^l \right\|_2^2 + \lambda \left\| \tilde{\boldsymbol{\rho}}^l \right\|_1, l = 1, 2, \cdots, L. \tag{19}$$

The target information can be estimated from the estimated $\tilde{\boldsymbol{\Theta}}$ by applying DFT to its rows. In practice, due to the influence of noise and clutters, we can hardly obtain the exact information of the targets and may yield false targets. In addition, the direct solution of (19) requires a high computational load and, thereby, may not be feasible for real-time processing.

It is seen that each row of the data matrix $\tilde{\mathbf{S}}_{cs}$ represents a series of measurements over successive pulses from the same virtual range bin. Therefore, the target Doppler frequencies can be estimated by the spectral analysis of the slow-time data for each virtual range bin. A simple technique is to conduct the DFT. Denote $\mathcal{F}(\bullet)$ as the DFT of "$\bullet$" in row vectors. We have

$$\begin{aligned} \mathcal{F}(\tilde{\mathbf{S}}_{cs}) &= \mathcal{F}(\tilde{\mathbf{M}} \tilde{\boldsymbol{\Theta}}) + \mathcal{F}(\tilde{\mathbf{N}}_{cs}) \\ &= \tilde{\mathbf{M}} \mathcal{F}(\tilde{\boldsymbol{\Theta}}) + \mathcal{F}(\tilde{\mathbf{N}}_{cs}) \end{aligned} \tag{20}$$

Each element of the matrix $\mathcal{F}(\tilde{\mathbf{S}}_{cs})$ is a Doppler spectrum sample corresponding to the virtual range bin and the frequency bin. As such, the Doppler spectrum samples can be used for target detection, i.e., determine whether a target is present at the virtual range bin and the Doppler bin.

The DFT acts as a matched filter for slow-time samples in the assumed scenarios. After DFT processing, the power of the k-th target becomes $2L^2 |\rho_k|^2 B_{cs}/B$ and the noise variance is $2LN_0 B_{cs}$. As such, the yielding SNR for the k-th target SNR_k^{DFT} is improved from the received SNR_k^{IN} by a factor of L. From the point of view of target detection, we can further improve the detection performance by matched filtering the sub-Nyquist samples corresponding to each Doppler bin. The details are discussed in the next section.

The detection process, however, only detects the existence of targets in a specific Doppler bin and does not
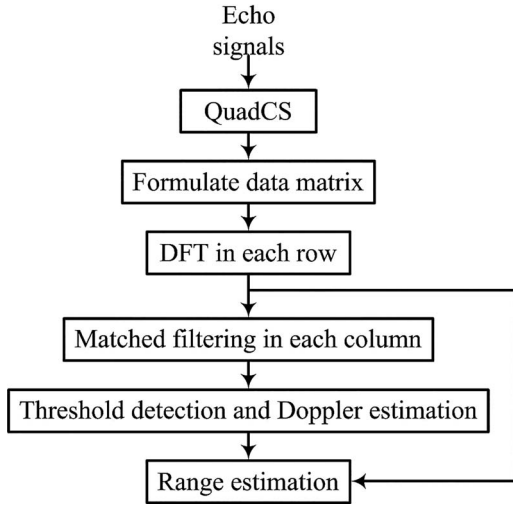
Echo
signals

$\downarrow$

| QuadCS |

$\downarrow$

| Formulate data matrix |

$\downarrow$

| DFT in each row |

$\downarrow$

| Matched filtering in each column |

$\downarrow$

| Threshold detection and Doppler estimation |

$\downarrow$

| Range estimation |

Fig. 4. Block schematic of CoSaPD processing.

DFT: $\left(\mathcal{F}(\tilde{\mathbf{S}}_{cs})\right)_{m,l} = \sum_{i=1}^{L} \left(\tilde{\mathbf{S}}_{cs}\right)_{m,i} \exp\left(-\mathrm{j}2\pi il \big/ L\right)$

Matched filtering:
$\tilde{\mathbf{M}}^{\mathrm{H}}\left(\mathcal{F}(\tilde{\mathbf{S}}_{cs})\right)^{l} = \tilde{\mathbf{M}}^{\mathrm{H}}\tilde{\mathbf{M}}\left(\mathcal{F}(\tilde{\mathbf{\Theta}})\right)^{l} + \tilde{\mathbf{M}}^{\mathrm{H}}\left(\mathcal{F}(\tilde{\mathbf{N}}_{cs})\right)^{l}$

Threshold detection & Doppler estimation:
For each Doppler bin l, targets exist if $\sum_{n=1}^{N}\mathrm{u}(|\tilde{x}_n| - T_D) \geq 1$.

Range estimation:
$\min_{\left(\mathcal{F}(\tilde{\mathbf{\Theta}})\right)^{l}} \frac{1}{2}\left\|\left(\mathcal{F}(\tilde{\mathbf{S}}_{cs})\right)^{l} - \tilde{\mathbf{M}}\left(\mathcal{F}(\tilde{\mathbf{\Theta}})\right)^{l}\right\|_2^2 + \lambda\left\|\left(\mathcal{F}(\tilde{\mathbf{\Theta}})\right)^{l}\right\|_1$
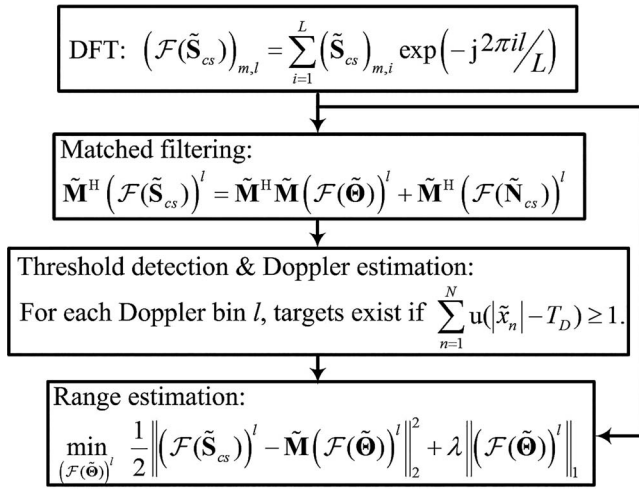
Fig. 5. Mathematical procedure of CoSaPD processing.

reveal the number of targets and their corresponding ranges. Note that the sparsity of $\mathcal{F}(\tilde{\mathbf{\Theta}})$ can be greatly enhanced even for practically nonsparse $\tilde{\mathbf{\Theta}}$ after performing the DFT. Therefore, for the underdetermined data $\tilde{\mathbf{S}}_{cs}$, we can estimate the number and the respective ranges of the targets by obtaining the sparse solution for each column of (20). Such estimation, however, requires a high computational load because the sparse estimation is performed for each column. Since we have already detected the targets from the Doppler spectrum samples, we only need to estimate the target ranges for the specific Doppler bins with detected targets. In this way, the computational load can be significantly reduced.

The block schematic of the processing steps involved in the CoSaPD processing is given in Fig. 4, and the mathematical procedure corresponding to the processing blocks is given in Fig. 5. It should be noted that the CoSaPD scheme must estimate the target velocities first and the ranges afterward, and this order cannot be reversed. The details of the detection process are depicted in the next section.

We now briefly discuss the Doppler estimation in the presence of clutter. Different from thermal noise, the clutter has a colored power spectrum as determined by the radar and the operation environment [1, 2, 28]. For a stationary transceiver, the clutter spectrum is around the zero Doppler frequency. In this case, as in classical pulse-Doppler processing, the CoSaPD scheme can isolate the clutter from the moving target. If the target is separable from the clutter spectrum, its detection is affected only by the thermal noise, but not the clutter. If the target is in the clutter-dominated area, on the other hand, the target is usually obscured by the clutter and cannot be detected. In this case, the Doppler spectrum samples in the contaminated area are simply discarded. However, because of clutter sidelobes, clutter power may spread over the entire Doppler frequencies, even though its power may be small at high Doppler frequencies. To reduce the sidelobe effects, we can add a data window [36] to weight the slow-time data for each virtual range bin prior to computing the DFT. With the windowed data, the clutter has a negligible effect on the estimation of targets as demonstrated by the simulated results in Section VI.

V.   THRESHOLD DETECTION AND ITS PERFORMANCE

This section describes the threshold detection used in the proposed CoSaPD processing and analyzes its performance.

Consider the l-th column which represents the Doppler bin data derived from (20) as

$$\left(\mathcal{F}(\tilde{\mathbf{S}}_{cs})\right)^{l} = \tilde{\mathbf{M}}\left(\mathcal{F}(\tilde{\mathbf{\Theta}})\right)^{l} + \left(\mathcal{F}(\tilde{\mathbf{N}}_{cs})\right)^{l}. \qquad (21)$$

Our objective is to detect if there exists one or more targets in the l-th Doppler bin, i.e., to determine if the vector $\left(\mathcal{F}(\tilde{\mathbf{\Theta}})\right)^{l}$ is a nonzero vector based on $\left(\mathcal{F}(\tilde{\mathbf{S}}_{cs})\right)^{l}$.

First, we assume that the received noise variance is known. For the data expressed in (21), we perform the following matched filtering to further enhance the detection performance,

$$\tilde{\mathbf{M}}^{\mathrm{H}}\left(\mathcal{F}(\tilde{\mathbf{S}}_{cs})\right)^{l} = \tilde{\mathbf{M}}^{\mathrm{H}}\tilde{\mathbf{M}}\left(\mathcal{F}(\tilde{\mathbf{\Theta}})\right)^{l} + \tilde{\mathbf{M}}^{H}\left(\mathcal{F}(\tilde{\mathbf{N}}_{cs})\right)^{l}, \quad (22)$$

which corresponds to the "matched filtering" operation in Fig. 4. For convenience, we define $\tilde{\mathbf{x}} = \tilde{\mathbf{M}}^{\mathrm{H}}\left(\mathcal{F}(\tilde{\mathbf{S}}_{cs})\right)^{l}$, $\tilde{\mathbf{y}} = \tilde{\mathbf{M}}^{\mathrm{H}}\tilde{\mathbf{M}}\left(\mathcal{F}(\tilde{\mathbf{\Theta}})\right)^{l}$, and $\tilde{\mathbf{w}} = \tilde{\mathbf{M}}^{\mathrm{H}}\left(\mathcal{F}(\tilde{\mathbf{N}}_{cs})\right)^{l}$. Then, (22) can be simplified as

$$\tilde{\mathbf{x}} = \tilde{\mathbf{y}} + \tilde{\mathbf{w}}. \qquad (23)$$

Note that the noise term $\tilde{\mathbf{w}}$ in (23) is Gaussian but not independent, as a result of the matched filtering. As illustrated in Section III, matrix $\tilde{\mathbf{M}}$ is approximately column-by-column orthogonal. Therefore, we can still assume that $\tilde{\mathbf{w}}$ is an IID Gaussian process. For the matched filter output expressed in (22), the peak power of the k-th target is $4L^2|\rho_k|^2 T_b^2 B_{cs}^4/B^2$ and the noise variance is $4LN_0 T_b B_{cs}^3/B$. As such, the SNR of the k-th target after
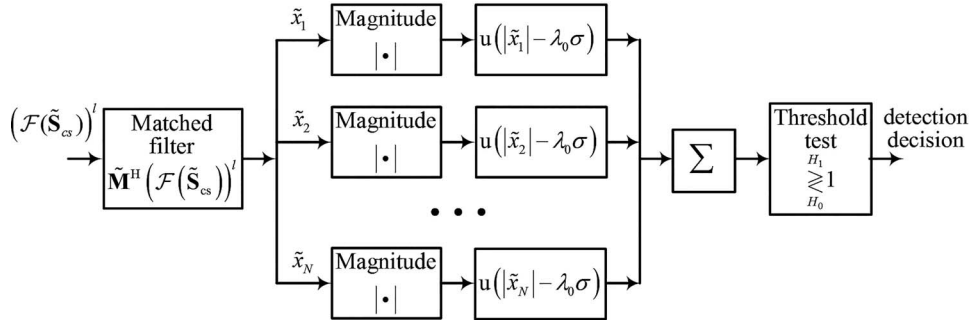
Fig. 6. Block schematic of detection process for Doppler bin.

the matched filtering, SNR_k^{MF}, becomes $T_b B_{cs} L$ times the received SNR_k^{IN}.

The detection problem is to detect the targets from data $\tilde{\mathbf{x}}$. The binary detection problem of each element $\tilde{x}_n$, $1 \leq n \leq N$, can be formulated as

$$
\begin{aligned}
H_0 &: |\tilde{x}_n| = |\tilde{w}_n| \\
H_1 &: |\tilde{x}_n| = |\tilde{y}_n + \tilde{w}_n|
\end{aligned}
\tag{24}
$$

The detection probability and false alarm probability are respectively given by

$$
P_D^n = \int_{T_D}^{\infty} f_{|\tilde{x}_n||H_1}(|\tilde{x}_n| \, | H_1) d \, |\tilde{x}_n|,
\tag{25}
$$

$$
P_F^n = \int_{T_D}^{\infty} f_{|\tilde{x}_n||H_0}(|\tilde{x}_n| \, | H_0) d \, |\tilde{x}_n|,
\tag{26}
$$

where T_D is the detection threshold, and $f_{|\tilde{x}_n||H_1}(|\tilde{x}_n| \, | H_1)$ and $f_{|\tilde{x}_n||H_0}(|\tilde{x}_n| \, | H_0)$ are the probability density functions (pdfs) of $|\tilde{x}_n|$ respectively for the cases when a target is present and absent. Then, the false alarm probability and the detection probability of $\tilde{\mathbf{y}}$ are respectively given by

$$
P_F \approx 1 - \prod_{n=1}^{N} (1 - P_F^n),
\tag{27}
$$

$$
P_D \approx 1 - \prod_{n=1}^{N} (1 - P_D^n).
\tag{28}
$$

Denote $\sigma^2 = 2L N_0 T_b B_{cs}^3 / B$ and notice that $|\tilde{w}_n|$ follows a Rayleigh distribution with mean $\sqrt{\pi/2}\sigma$ and variance $(4 - \pi)\sigma^2/2$. Under hypothesis H_0, i.e., a target is absent, the conditional pdf of $|\tilde{x}_n|$ is given by

$$
f_{|\tilde{x}_n||H_0}(|\tilde{x}_n| \, | H_0) = \frac{|\tilde{x}_n|}{\sigma^2} \exp\left(-\frac{|\tilde{x}_n|^2}{2\sigma^2}\right).
\tag{29}
$$

Under hypothesis H_1, i.e., when a target is present, $\tilde{x}_n = \tilde{y}_n + \tilde{w}_n$ is complex Gaussian distributed with mean $\tilde{y}_n$ and variance $2\sigma^2$. Then, the pdf of $|\tilde{x}_n|$ follows the Rician distribution, expressed as

$$
\begin{aligned}
&f_{|\tilde{x}_n||H_1}(|\tilde{x}_n| \, | H_1) \\
&= \frac{|\tilde{x}_n|}{\sigma^2} \exp\left(-\frac{|\tilde{x}_n|^2 + |\tilde{y}_n|^2}{2\sigma^2}\right) I_0\left(\frac{|\tilde{x}_n||\tilde{y}_n|}{\sigma^2}\right),
\end{aligned}
\tag{30}
$$

where $I_0(\bullet)$ is the modified Bessel function of the first kind [37].

With the known noise power σ^2, the Neyman-Pearson optimal detector can be derived from the likelihood ratio test as

$$
\frac{f_{|\tilde{x}_n||H_1}(|\tilde{x}_n| \, | H_1)}{f_{|\tilde{x}_n||H_0}(|\tilde{x}_n| \, | H_0)} = \exp\left(-\frac{|\tilde{y}_n|^2}{2\sigma^2}\right) I_0\left(\frac{|\tilde{x}_n||\tilde{y}_n|}{\sigma^2}\right) \underset{H_0}{\overset{H_1}{\gtrless}} \lambda.
\tag{31}
$$

Because $I_0(\bullet)$ is a monotonically increasing function, (31) is equivalent to the following simpler expression,

$$
|\tilde{x}_n| \underset{H_0}{\overset{H_1}{\gtrless}} \lambda_0 \sigma = T_D,
\tag{32}
$$

where $\lambda_0 = \sqrt{-2 \ln(P_F^n)}$ is the scale factor used to control the false alarm rate. Thus, we can derive the joint detector for a vector data $\tilde{\mathbf{x}}$ as

$$
\sum_{n=1}^{N} u\left(|\tilde{x}_n| - \lambda_0 \sigma\right) \underset{H_0}{\overset{H_1}{\gtrless}} 1,
\tag{33}
$$

where $u(\bullet)$ represents the unit step function. The detection process for a Doppler bin is shown in Fig. 6.

From (26), (29), and (32), we can derive $P_F^n = \exp(-\lambda_0^2/2)$. Then, the false alarm probability is obtained as

$$
P_F \approx 1 - \left(1 - \exp(-\lambda_0^2/2)\right)^N.
\tag{34}
$$

We are unable to derive a closed-form expression of the detection probability P_D. However, it is noted that the processing gain of the CoSaPD detector is $T_b B_{cs} L$, which is smaller than the gain of classical processing, $T B_b L$. Therefore, it is expected that the performance of the proposed detector will be inferior when compared with the classical detector at the low SNR region.

After target detection, the CoSaPD processing conducts range estimation through the sparse recovery algorithms, as discussed in the previous section. As is well known, an inherent characteristic of the sparse recovery algorithms [38, 39] is to detect the nonzero elements in a sparse vector. To improve the system detection performance, we may set a low detection threshold for each Doppler bin. However, a low threshold will increase the false alarm probability and thus may introduce false targets. Nevertheless, false targets can be removed through

the detection process in the recovery algorithms. Because the sparse recovery algorithms strive for a minimum number of nonzero cells at its output, from the system point of view, the false alarm probability of the radar system does not increase despite the low detection threshold. This observation is verified later through simulations.

In practice, it is impossible to know the noise parameter σ in advance. To maintain a CFAR, therefore, we should estimate parameter σ so as to determine an adaptive threshold for detection. Following the assumptions on the measurement matrix $\tilde{\mathbf{M}}$, it is seen that the noise matrix $\tilde{\mathbf{M}}^{\mathrm{H}}\mathcal{F}(\tilde{\mathbf{N}}_{cs})$ is IID, and the absolute value of each element $|(\tilde{\mathbf{M}}^{\mathrm{H}}\mathcal{F}(\tilde{\mathbf{N}}_{cs}))_{i,j}|$, $1 \leq i \leq N$, $1 \leq j \leq L$, follows the Rayleigh distribution. As such, the maximum likelihood estimate of σ is simply the average of the available data [40], expressed as

$$\hat{\sigma} = \sqrt{\frac{2}{\pi}} \frac{\sum\limits_{(i,j)\in\Lambda} \left|(\tilde{\mathbf{M}}^{\mathrm{H}}\mathcal{F}(\tilde{\mathbf{N}}_{cs}))_{i,j}\right|}{|\Lambda|} \tag{35}$$

where Λ is the set consisting of all available i and j, and $|\Lambda|$ is its cardinality. For sparse targets, the accumulative strength of the signals $\sum\limits_{(i,j)\in\Lambda} |(\tilde{\mathbf{M}}^{\mathrm{H}}\tilde{\mathbf{M}}\mathcal{F}(\tilde{\boldsymbol{\Theta}}))_{i,j}|$ is much smaller than that of the noise $\sum\limits_{(i,j)\in\Lambda} |(\tilde{\mathbf{M}}^{\mathrm{H}}\mathcal{F}(\tilde{\mathbf{N}}_{cs}))_{i,j}|$, and the following approximation holds when $|\Lambda|$ is large:

$$\frac{\sum\limits_{(i,j)\in\Lambda} \left|(\tilde{\mathbf{M}}^{\mathrm{H}}\mathcal{F}(\tilde{\mathbf{N}}_{cs}))_{i,j}\right|}{|\Lambda|} \approx \frac{\sum\limits_{(i,j)\in\Lambda} \left|(\tilde{\mathbf{M}}^{\mathrm{H}}\mathcal{F}(\tilde{\mathbf{S}}_{cs}))_{i,j}\right|}{|\Lambda|}. \tag{36}$$

In the simulation study, we set $|\Lambda| = NL$ and the estimated $\hat{\sigma}$ becomes

$$\hat{\sigma} \approx \sqrt{\frac{2}{\pi}} \frac{\sum\limits_{i=1}^{N}\sum\limits_{j=1}^{L} \left|(\tilde{\mathbf{M}}^{\mathrm{H}}\mathcal{F}(\tilde{\mathbf{S}}_{cs}))_{i,j}\right|}{NL}, \tag{37}$$

and the detection threshold is given as $T_D = \lambda_0 \hat{\sigma}$.

VI. SIMULATIONS

In this section, we present the simulation performance of the proposed CoSaPD processing and compare it with classical processing [1, 2] and direct processing by (19). Subsection VI-A introduces the simulation scenarios. Subsections VI-B and VI-C respectively provide simulated results of the detection and estimation performance in an AWGN environment. The effects of clutter are examined in Subsection VI-D.

A. Simulation Scenarios

It is assumed that the radar transmits a linear frequency modulation pulse train with carrier frequency $f_c = 10$ GHz, signal bandwidth $B = 200$ MHz, pulsewidth $T_b = 10^{-5}$ s, and PRI $T = 10^{-4}$ s. The CPI consists of $L = 100$ pulses. For the assumed parameters, the unambiguous target ranges and Doppler frequencies are 1500 m $\sim$ 3466.5 m and -5 KHz $\sim$ 5 KHz,
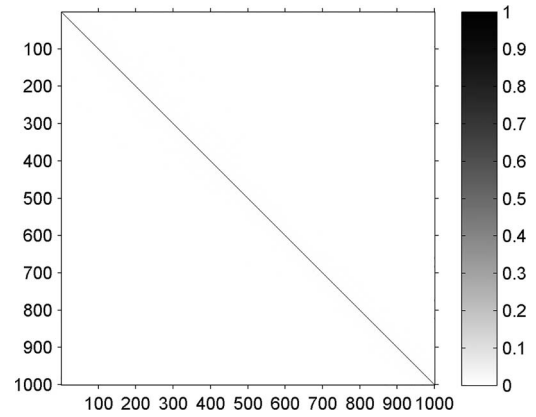

Fig. 7. Distribution of averaged Gram matrix $\tilde{\mathbf{M}}^{\mathrm{H}}\tilde{\mathbf{M}}$.

respectively. The range resolution is 0.75 m and the Doppler resolution is 0.1 KHz.

For the QuadCS system, the chipping sequence $p(t)$ is generated by random ± 1s with rate $1/B$ and the bandpass filter is set to be an ideal one with bandwidth B_{cs}. Two bandpass filters with $B_{cs} = 50$ MHz and $B_{cs} = 25$ MHz are respectively considered. For the two filters, the sampling rates are one-fourth and one-eighth of the Nyquist rate, respectively. The basis BPDN algorithm [31] is used for the sparse target recovery.

A flat power spectrum is assumed in the simulated radar signal. The QuadCS measurement matrix $\tilde{\mathbf{M}}$ is approximately column-by-column orthogonal. Fig. 7 shows the distribution of the averaged Gram matrix $\tilde{\mathbf{M}}^{\mathrm{H}}\tilde{\mathbf{M}}$ over 1000 independent trials for $B_{cs} = 25$ MHz. The maximum off-diagonal element of the Gram matrix is 0.015, thus clearly verifying the reasonableness of the assumption.

B. Detection Performance

Assume three targets with the same SNR. The target delays and the Doppler frequencies are randomly set in the unambiguous region. We present three simulation examples. For the first two examples, the delays and the Doppler frequencies are on the resolution grids. For the third example, the delays and the Doppler frequencies are arbitrarily set. To examine the detectability of the multiple targets, their Doppler frequencies are set to fall in the same Doppler bin. All results are obtained by averaging over 1000 independent trials.

First, we show that the CoSaPD detector achieves a CFAR in a Doppler bin. Fig. 8 shows the variations of the false alarm probability versus the scale factor for different values of SNR when $B_{cs} = 25$ MHz. It is clear that the change of the noise power does not affect the false alarm probability for a specified scale factor, which is consistent with the theoretical result given in (34). The same conclusion can be drawn for $B_{cs} = 50$ MHz.

Next, we examine the receiver operating characteristic (ROC) of the CoSaPD detector. Fig. 9 compares the averaged ROC curves obtained by the CoSaPD and the
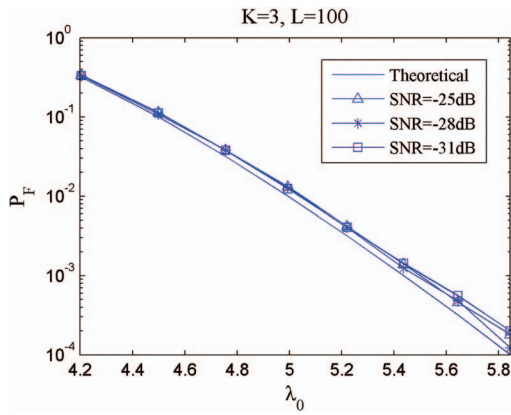
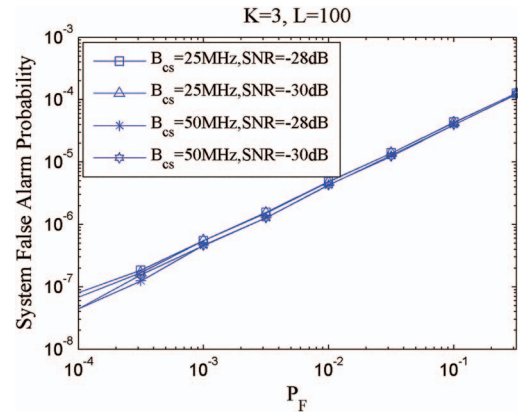Fig. 8. False alarm probability versus scale factor.

Fig. 10. System false alarm probability versus detector false alarm probability.
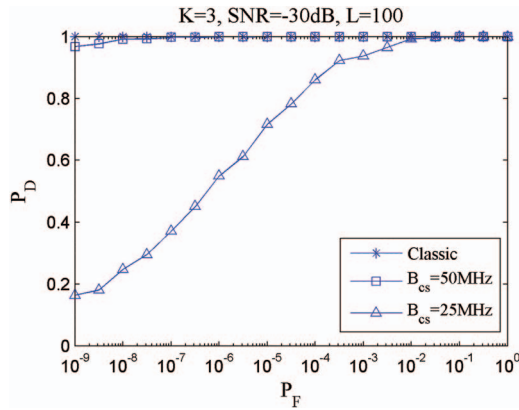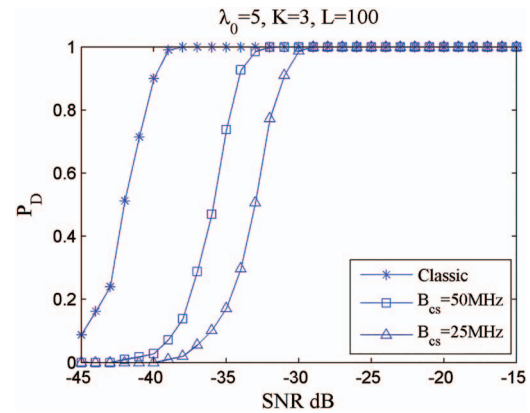

Fig. 9. ROC of CoSaPD detector.

Fig. 11. Detection performance versus SNR.

classical processing. It is seen that the performance of the CoSaPD detector is inferior to the classical detector due to the decrease of the SNR gains. In the Nyquist-rate case, after the matched filtering and DFT processing, the processing gain can achieve $T_b B L$, while the QuadCS system only realize a gain of $T_b B_{cs} L$. As the bandpass width B_{cs} increases, the processing gain $T_b B_{cs} L$ increases and then the detection performance is enhanced. In the simulated example, processing gains of 53 dB, 47 dB, and 44 dB are respectively achieved for classical processing, CoSaPD detector with $B_{cs} = 50$ MHz, and that with $B_{cs} = 25$ MHz. The yielding SNRs for detection are 23 dB, 17 dB, and 14 dB, respectively, implying an SNR reduction of 6 dB and 9 dB for the CoSaPD with $B_{cs} = 50$ MHz and $B_{cs} = 25$ MHz cases as compared with the classical processing. For $B_{cs} = 50$ MHz, i.e., when the compressive sampling rate equals one-fourth of the Nyquist rate, the detection performance of the CoSaPD detector is close to that of the classical detector in the simulated range of P_F.

As discussed in the previous section and noted in Fig. 9, we can choose a high false alarm probability to increase the detection probability. Reduction of false targets can be achieved in the recovery stage of the target range following the detector, because the sparse recovery algorithm has the inherent target detection ability [38, 39].

Fig. 10 shows the false alarm rate of the system after the recovery stage versus that of the detector. It is clear that although the detector has a high false alarm probability in the detection stage, the recovery algorithm can keep the system having a low false alarm probability. Processing the system detection in this way will slightly increase the computational burden in the range estimation.

Fig. 11 further shows the detection performance with respect to the SNR for the case of $P_F = 10^{-2}$. It is seen that even at a low SNR of -30 dB, the CoSaPD detector can approach the performance of the classical detector with the data rate being only one-eighth of the Nyquist rate.

Finally, we consider a realistic scenario in which the ranges and Doppler frequencies of the targets are continuous and thus may not fall on the resolution grids. Fig. 12 shows the ROC in this case. In comparison with Fig. 9, the detection performance degrades. It is noted that when a target is not on Doppler bin grids, the detected target energy is from the Doppler leakage and thus is smaller than that of the target on the Doppler bin. When the target is off from the range bin grids, the measurement matrix contains errors, which will degenerate the matched filter in (22). In this case, the detection performance is compromised as compared with the case that the targets are on the resolution grids.
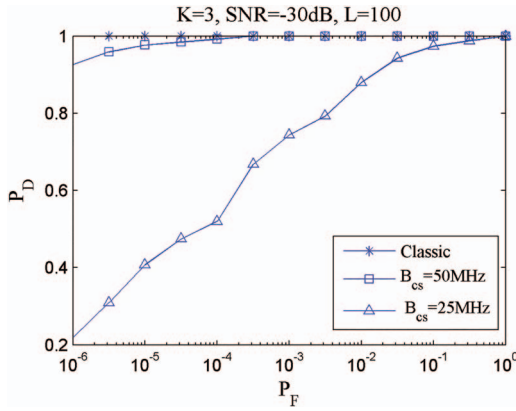
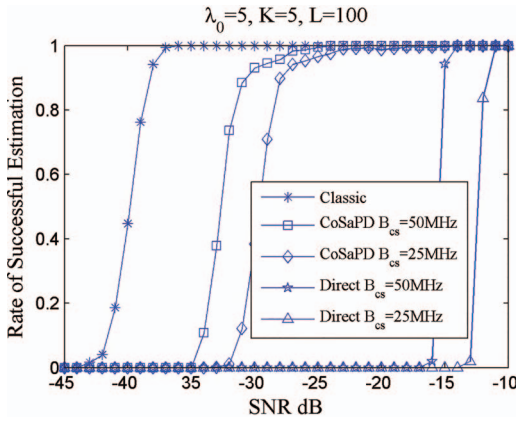Fig. 12.   ROC in realistic case.

Fig. 14.   Times of recovery algorithms required for range estimation.

Fig. 13.   Rates of successful estimation for different methods.
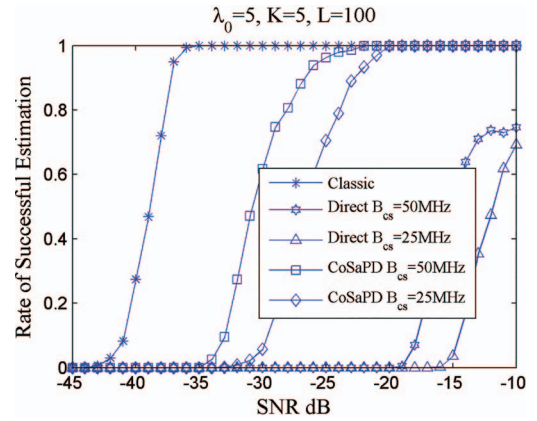
Fig. 15.   Rate of successful estimation in practical scenario.

C.   Estimation Performance

After detecting the existence of the targets in a specific Doppler bin, we estimate the corresponding target ranges. The CoSaPD method is depicted in the last stage of Fig. 5 and is realized through the sparse recovery algorithms. The rate of successful estimation is used as the performance metric. When the targets are on the resolution grids, a successful estimation refers to the correct estimation of both ranges and Doppler frequencies. On the other hand, when the target ranges and Doppler frequencies are chosen randomly at the unambiguous region, a successful estimation is declared if both differences between the estimated and true ranges and Doppler frequencies are smaller than half of the respective cell resolution.

In the simulation studies, we consider five targets with the same SNRs. To examine the discrimination capability, we assume that the first two targets belong to the same range bin, the other two targets belong to another Doppler bin, and the fifth target is chosen to have random range and Doppler. All results are obtained by averaging over 1000 independent trials.

First, we depict the estimation performance when all five targets are set on the discrete grids. Fig. 13 shows the rates of successful estimation with respect to the input SNR. For the CoSaPD method, the false alarm probability is set as $P_F = 10^{-2}$ with $\lambda_0 = 5$. It is seen that the
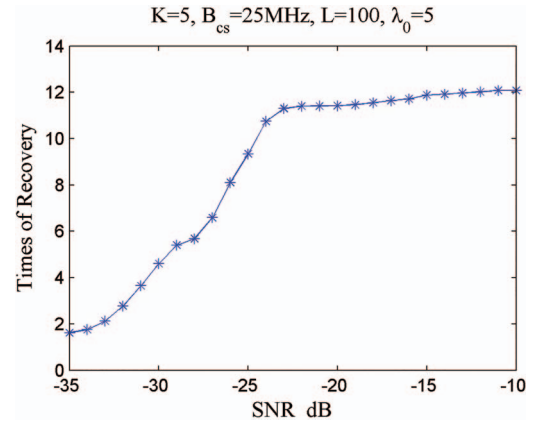
CoSaPD method greatly outperforms the direct method and achieves the performance of the classical method even at a low SNR of -25 dB and the sampling rate is only one-eighth of the Nyquist rate. The performance improvement of the CoSaPD method is due to the fact that the range estimation is performed in the Doppler domain in which the SNR is enhanced because of the DFT processing. Setting $P_F = 10^{-2}$ will result in a high false alarm probability in the detection stage. However, the setting does not affect the system detection.

Another advantage of the CoSaPD method over the direct processing method is the reduction of the computational burden. For the simulated parameters, the direct method needs to execute the recovery algorithms for 100 times, whereas the CoSaPD method only needs at most 12 times, as shown in Fig. 14.

Next, we present the simulated performance when the target ranges and Doppler frequencies are randomly set in the unambiguous region. Fig. 15 shows the rates of successful estimation. Compared with Fig. 13, the estimated performance degrades. However, the CoSaPD method is more applicable to realistic situations than the direct processing method. As discussed in Section IV, the direct processing method first estimates the complex amplitudes of the targets from the compressed data. The estimation may introduce errors in both amplitude and
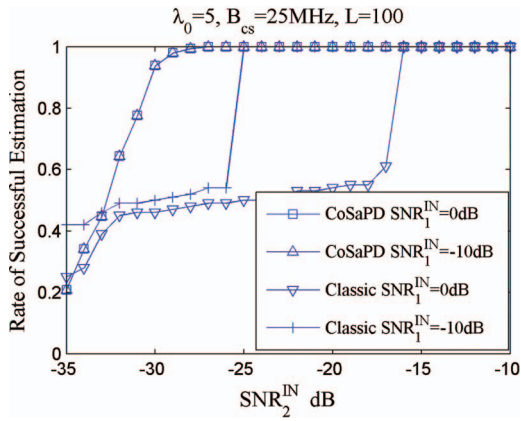
Fig. 16. Estimation performance of smaller target.

Fig. 17. Rates of successful estimation in clutter for discarding (a) 5 Doppler bins and (b) 13 Doppler bins.

phase. In particular, the phase error will greatly affect the Doppler estimation in the DFT operation, thus causing performance degradation to the direct processing method. For the CoSaPD method, the Doppler estimation is performed in the Doppler domain data, which is obtained from the DFT of the compressive data. As such, it yields a robust range estimate unaffected by the Doppler phase.

Finally, we simulate the performance of estimating a weak target that is close to a strong one. In the classical processing, the output of the matched filtering will have sidelobes in range, making the weak target obscured by the sidelobes of the strong target. We assume that the two targets are present in the same Doppler bin and the weak target is randomly set in the first sidelobe of the strong target. Fig. 16 shows the estimation performance, where SNR_1^{IN} and SNR_2^{IN} denote the SNRs of the strong and the weak targets, respectively. It is observed that the CoSaPD method outperforms the classical method when the two targets have a large SNR difference.

D.   The Effects of Clutter

We now demonstrate the performance of the CoSaPD processing in the presence of surface clutter. The received target signals are contaminated by both noise and clutter as described in (5). The signals and noise are set as in Fig. 13 and the simulated windblown ground clutter is added. The ground clutter is assumed to be Rayleigh distributed in amplitude and obeys the following two-sided exponential law in Doppler spreading

$$S_c(v) = \frac{\beta}{2} \exp(-\beta |v|), \ -\infty < v < \infty,$$

where β corresponds to the wind conditions. It was shown in [28] that the Doppler model matches the measured shapes of windblown ground clutter Doppler spectra much more closely than by the Gaussian or power-law approximations. In the simulation, we choose $\beta = 4.3$, which corresponds to a wind condition of about 96.6 km/hr. The SCR is -40 dB. To reduce the effect of clutter, a Taylor window, which yields 10 nearly constant-level sidelobes adjacent to the mainlobe with a
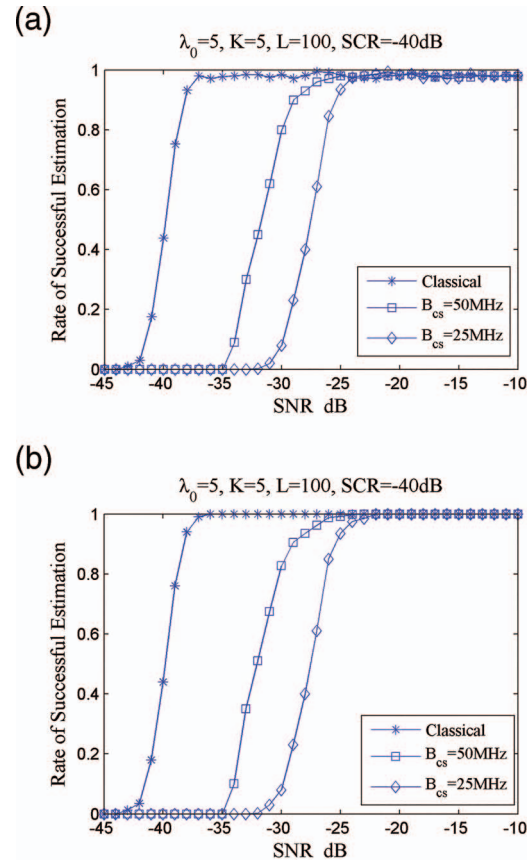
peak sidelobe level of -70 dB relative to the mainlobe peak, is used before DFT processing.

As discussed in Section IV, the Doppler spectrum samples are discarded if the targets fall in the clutter-dominated area. We evaluate the rates of successful estimation at different SNR levels after discarding different Doppler bins around the zero Doppler frequency. Fig. 17(a) and Fig. 17(b) show the simulated results after discarding 5 and 13 Doppler bins, respectively. The effect of the clutter is evident from Fig. 17(a). Because of clutter sidelobe, we cannot obtain 100% successful estimation rates for both classical and CoSaPD methods. By discarding more Doppler bins, as shown in Fig. 17(b), we can better remove the clutter effect on the signals with high Doppler shifts. Fig. 18 further shows the usable Doppler space fraction [2] versus the SNR. In the simulations, we set one target with a randomly distributed range bin and a variable Doppler bin. When the target is successfully estimated, we claim the Doppler bin to be usable. It is seen that there is sharp drop of the usable Doppler space when the SNR is below some threshold. This is because the recovery algorithms do not function in such low SNRs.[2] Both Fig. 17(b) and Fig. 18 indicate that

---

[2] The l_1-norm minimization algorithms in a noisy signal case yield sparse solutions only when $\|(\mathcal{F}(\tilde{N}_{cs}))^i\|_2^2 < \|(\mathcal{F}(\tilde{S}_{cs}))^i\|_2^2$ [41].
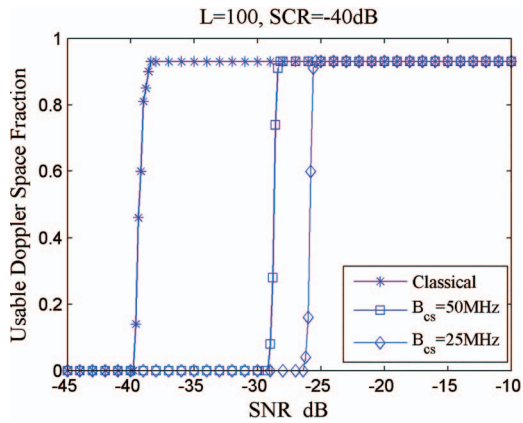
Fig. 18.   Usable Doppler space fraction versus SNR.

the CoSaPD method achieves the performance of the classical method even at an SNR of -25 dB and a data rate of one-eighth of the Nyquist rate. This is consistent with the observation made in Fig. 13.

VII.   CONCLUSION

In this paper, we have developed a pulse-Doppler processing scheme, termed as CoSaPD, with the sub-Nyquist data delivered from the QuadCS system. The scheme consists of two major procedures, Doppler estimation/detection and range estimation, with the former to be performed prior to the latter. Theoretical analyses and computer simulation results verify the performance advantages of the proposed CoSaPD approach. When sampling at one-eighth of the Nyquist rate and for SNR above -25 dB, the CoSaPD achieves the performance of the classical processing using Nyquist samples.

When compared with other related schemes utilizing CS data, the proposed CoSaPD scheme offers four important advantages. The first one is the small size dictionary. While other CS-based radar data processing schemes usually use a two-dimensional dictionary by discretizing both radar range and Doppler [23], the CoSaPD scheme adopts a one-dimensional dictionary by only discretizing the radar range. The second advantage is the combination of the estimation and detection processes, which has two advantages over separate estimation and detection: improved detection performance and reduced computational complexity. The third advantage is its ability to detect weak targets nearby a strong target. The last one is the ability to cancel the clutter echoes as in classical processing.

In comparison with the classical processing, the CoSaPD produces the system gain loss. As discussed in Section V, the CoSaPD processing gain is B_{cs}/B times that of the classical processing. That is, a narrow bandwidth B_{cs} and, hence, a low sampling rate f_{IF}^{cs}, yields large processing gain losses. There is a trade-off between the unacceptable loss and the sampling rate.

REFERENCES

[1]   Richards, M. A.
        Fundamentals of Radar Signal Processing. New York: McGraw-Hill, 2005.

[2]   Richards, M. A., Scheer, J. A., and Holm, W. A.
        Principles of Modern Radar: Basic Principles. Raleigh, NC: Scitech Publishing, 2010.

[3]   Ho, K. C., Chan, Y. T., and Inkol, R.
        A digital quadrature demodulation system.
        IEEE Transactions on Aerospace and Electronic Systems, **32**, 4 (Oct. 1996), 1218–1227.

[4]   Liu, H., Ghafoor, A., and Stockmann, P. H.
        A new quadrature sampling and processing approach.
        IEEE Transactions on Aerospace and Electronic Systems, **25**, 5 (Sep. 1989), 733–748.

[5]   Vaughan, R. G., Scott, N. L., and White, D. R.
        The theory of bandpass sampling.
        IEEE Transactions on Signal Processing, **39**, 9 (Sep. 1991), 1973–1984.

[6]   Donoho, D. L.
        Compressed sensing.
        IEEE Transactions on Information Theory, **52**, 4 (Apr. 2006), 1289–1306.

[7]   Baraniuk, R. G.
        Compressive sensing.
        IEEE Signal Processing Magazine, **24**, 4 (Jul. 2007), 118–121.

[8]   Candes, E. J., Romberg, J., and Tao, T.
        Robust uncertainty principles: Exact signal reconstruction from highly incomplete frequency information.
        IEEE Transactions on Information Theory, **52**, 2 (Feb. 2006), 489–509.

[9]   Laska, J., Kirolos, S., Massoud, Y., Baraniuk, R., Gilbert, A., Lwen, M., and Strauss, M.
        Random sampling for analog-to-information conversion of wideband signals.
        IEEE Dallas Workshop on Design, Applications, Integration and Software, Oct. 2006, pp. 119–122.

[10]   Laska, J. N., Kirolos, S., Duarte, M. F., Ragheb, T. S., Baraniuk, R. G., and Massoud, Y.
        Theory and implementation of an analog-to-information converter using random demodulation.
        IEEE International Symposium on Circuits and Systems, May 27–30, 2007, pp. 1959–1962.

[11]   Tropp, J. A., Laska, J. N., Duarte, M. F., Romberg, J. K. and Baraniuk, R. G.
        Beyond Nyquist: Efficient sampling of sparse bandlimited signals.
        IEEE Transactions on Information Theory, **56**, 1 (Jan. 2010), 520–544.

[12]   Yoo, J., Turnes, C., Nakamura, E. B., Le, C. K., Becker, S., Sovero, E. A., Wakin, M. B., Grant, M. C., Romberg, J., Emami-Neyestanak, A., and Candes, E.
        A compressed sensing parameter extraction platform for radar pulse signal acquisition.
        IEEE Journal on Emerging and Selected Topics in Circuits and Systems, **2**, 3 (Sep. 2012), 626–638.

[13]   Taheri, O., and Vorobyov, S. A.
        Segmented compressed sampling for analog-to-information conversion: Method and performance analysis.
        IEEE Transactions on Signal Processing, **59**, 2 (Feb. 2011), 554–572.

[14]   Mishali, M., Elder, Y. C., Dounaevsky, O., and Shoshan, E.
        Xampling: Analog to digital at sub-Nyquist rates.
        IET Circuits, Devices and Systems, **5**, 1 (Jan. 2011), 8–20.

[15]   Xi, F., Chen, S. Y., and Liu, Z.
        Quadrature compressive sampling for radar echo signals.

2011 International Conference on Wireless Communications and Signal Processing, Nov. 1–5, 2011, pp. 1–5.

[16] Xi, F., Chen, S. Y., and Liu, Z.
Quadrature compressive sampling for radar signals.
IEEE Transactions on Signal Processing, **62**, 11 (Jun. 2014), 2787–2802.

[17] Shi, G. M., Lin, J., Chen, X. Y., Qi, F., Liu, D. H., and Zhang, L.
UWB echo signal detection with ultra-low rate sampling based on compressed sensing.
IEEE Transactions on Circuits and Systems II: Express Briefs, **55**, 4 (Apr. 2008), 379–383.

[18] Davenport, M. A., Boufounos, P. T., Wakin, M. B., and Baraniuk, R. G.
Signal processing with compressive measurements.
IEEE Journal on Selected Topics in Signal Processing, **4**, 2 (Apr. 2010), 445–460.

[19] Bajwa, W. U., and Pezeshki, A.
Finite frames for sparse signal processing.
In *Finite Frames: Theory and Applications*, P. Casazza, and G. Kutyniok, Eds. Boston: Birkhauser, 2013.

[20] Anitori, L., Maleki, A., Otten, M., Baraniuk, R. G., and Hoogeboom, P.
Design and analysis of compressed sensing radar detectors.
IEEE Transactions on Signal Processing, **61**, 4 (Feb. 2013), 813–827.

[21] Pollock, B., and Goodman N. A.
Detection performance of compressively sampled radar signals.
IEEE Radar Conference, May 23–27, 2011, pp. 1117–1122.

[22] Kyriakides, I.
Adaptive compressive sensing and processing of delay-Doppler radar waveforms.
IEEE Transactions on Signal Processing, **60**, 2 (Feb. 2012), 730–739.

[23] Herman, M. A., and Strohmer, T.
High-resolution radar via compressed sensing.
IEEE Transactions on Signal Processing, **57**, 6 (Jun. 2009), 2275–2284.

[24] Smith, G. E., Diethe, T., Hussian, Z., Shawe-Taylor, J., and Hardoon, D. R.
Compressed sampling for pulse Doppler radar.
IEEE Radar Conference, May 10–14, 2010, pp. 887–892.

[25] Bajwa, W. U., Gedalyahu, K., and Eldar, Y. C.
Identification of parametric underspread linear systems and super-resolution radar.
IEEE Transactions Signal Processing, **59**, 6 (Jun. 2011), 2548–2561.

[26] Baransky, E., Itzhak, G., Shmuel, I., Wagner, N., Shoshan, E., and Elder, Y. C.
A sub-Nyquist radar prototype: Hardware and algorithms.
IEEE Transactions on Aerospace and Electronic Systems, **50**, 2 (Apr. 2014), 809–822.

[27] Bar-Ilan, O., and Elder, Y. C.
Sub-Nyquist radar via Doppler focusing.
IEEE Transactions on Signal Processing, **62**, 7 (Apr. 2014), 1796–1811.

[28] Billingsley, J. B. *Low-Angle Radar Land Clutter: Measurements and Empirical Models.* Norwich, NY: William Andrew Publishing, 2002.

[29] Candes, E. J., and Tao, T.
Decoding by lineal programming.
IEEE Transactions on Information Theory, **51**, 12 (Dec. 2005), 4203–4215.

[30] Xi, F., Chen, S. Y., and Liu, Z.
Quardrature compressive sampling for radar signals: Output noise and robust reconstruction.
2014 IEEE China Summit and International Conference on Signal and Information Processing, Jul. 9–13, 2014.

[31] Chen, S. S., Donoho, D. L., and Saunders M. A.
Atomic decomposition by basis pursuit.
SIAM Journal on Scientific Computing, **20**, 1 (1998), 33–61.

[32] Tropp, J. A., and Gilbert, A. C.
Signal recovery from random measurements via orthogonal matching pursuit.
IEEE Transactions on Information Theory, **53**, 12 (Dec. 2007), 4655–4666.

[33] Needell, D., and Vershynin, R.
Signal recovery from incomplete and inaccurate measurements via regularized orthogonal matching pursuit.
IEEE Journal of Selected Topics in Signal Processing, **4**, 2 (Apr. 2010), 310–316.

[34] Tibshirani, R.
Regression shrinkage and selection via the lasso.
Journal of the Royal Statistical Society. Series B, **58**, 1 (1996), 267–288.

[35] Fornasier, M.
Numerical methods for sparse recovery.
Radon Series on Computational and Applied Mathematics, **9**, 2010, 1–110.

[36] Harris, F. J.
On the use of windows for harmonic analysis with the discrete Fourier transform.
Proceedings of the IEEE, **66**, 1 (Jan. 1978), 51–83.

[37] Abramowitz, M., and Stegun, I. A.
Handbook of Mathematical Functions with Formulas, Graphs, and Mathematical Tables. National Bureau of Standards, U.S. Dept. of Commerce, 1972.

[38] Stojnic, M.
$\ell 1$ optimization and its various thresholds in compressed sensing.
2010 IEEE International Conference on Acoustics Speech and Signal Processing, Mar. 14–19, 2010, pp. 3910–3913.

[39] Fuchs, J. J.
The generalized likelihood ratio test and the sparse representations approach.
International Conference on Image and Signal Processing, 2010, pp. 245–253.

[40] Kay, S. M. *Fundamentals of Statistical Signal Processing, Vol. I: Estimation Theory.* Upper Saddle River, NJ: Prentice-Hall, 1993.

[41] Hennenfent, G., van den Berg, E., Friedlander, M. P., and Herrmann, F.
New insights into one-norm solvers from the Pareto curve.
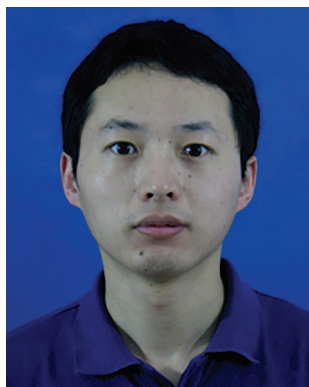*Geophysics*, **73**, 4 (Jul. 2008), A23–A26.

Chao Liu received the B.S. degree in electronic science and technology from Nanjing University of Information Science and Technology, Nanjing, China, in 2006.

He is currently pursuing his Ph.D. degree in the Department of Electronic Engineering, Nanjing University of Science and Technology, Nanjing, China. His research interests include radar signal processing and compressive sensing.

Feng Xi (M'14) received the B.S. degree in electrical engineering and the Ph.D. degree in information and communication engineering from Nanjing University of Science and Technology, Nanjing, China, in 2003 and 2010, respectively.

Currently, he is an Associate Professor in the Department of Electrical Engineering, Nanjing University of Science and Technology, Nanjing, China. His research interests include radar signal processing, chaotic dynamical system, and wireless sensor networks.

Shengyao Chen (M'14) received the B.S. degree in communication engineering and the Ph.D. degree in information and communication engineering from Nanjing University of Science and Technology, Nanjing, China, in 2006 and 2013, respectively.

He is now a Post-Doctoral Research Fellow at Nanjing University of Science and Technology, Nanjing, China. His research interests include radar and communication systems, signal processing, and chaotic dynamical systems.

Yimin D. Zhang (SM'01) received his Ph.D. degree from the University of Tsukuba, Tsukuba, Japan, in 1988.

He joined the faculty of the Department of Radio Engineering, Southeast University, Nanjing, China, in 1988. He served as a Director and Technical Manager at the Oriental Science Laboratory, Yokohama, Japan, from 1989 to 1995, and a Senior Technical Manager at the Communication Laboratory Japan, Kawasaki, Japan, from 1995 to 1997. He was a Visiting Researcher at the ATR Adaptive Communications Research Laboratories, Kyoto, Japan, from 1997 to 1998. Since 1998, he has been with Villanova University, Villanova, PA, USA, where he is currently a Research Professor with the Center for Advanced Communications, and is the Director of the Wireless Communications and Positioning Laboratory and the Director of the Radio Frequency Identification (RFID) Laboratory. His general research interests lie in the areas of statistical signal and array processing for radar, communications, and navigation applications, including compressive sensing, convex optimization, nonstationary signal and time-frequency analysis, MIMO systems, radar imaging, target localization and tracking, wireless and cooperative networks, and jammer and clutter suppression.

Dr. Zhang has 11 book chapters and more than 250 journal articles and peer-reviewed conference papers. He serves on the Editorial Board of the *Signal Processing* journal. He was an Associate Editor for the *IEEE Transactions on Signal Processing* during 2010–2014, an Associate Editor for the *IEEE Signal Processing Letters* during 2006–2010, and an Associate Editor for the *Journal of the Franklin Institute* during 2007–2013. He is a member of the Sensor Array and Multichannel (SAM) Technical Committee of the IEEE Signal Processing Society. He is a Technical Committee Co-chair of the IEEE Benjamin Franklin Symposium on Microwave and Antenna Sub-systems in 2014.

Zhong Liu (M'03) received the B.S. degree from Anhui University, Hefei, Anhui, China, in 1983 and the M.S. and Ph.D. degrees from the University of Electronic Science and Technology of China, Chengdu, Sichuan, China, in 1985 and 1988, all in electrical engineering.

He was a Postdoctoral Fellow at Kyoto University, Kyoto, Japan, from 1991 to 1993. He was a Researcher at the Chinese University of Hong Kong, Hong Kong, from 1997 to 1998. Currently, he is a Professor at the Department of Electronic Engineering, Nanjing University of Science and Technology, Nanjing, Jiangsu, China. His research interests include chaos and information dynamics, signal processing, radar, and communication technologies.